

Eutectic colony formation: A phase-field studyMathis Plapp^{1,2} and Alain Karma¹¹*Physics Department and Center for Interdisciplinary Research on Complex Systems, Northeastern University, Boston, Massachusetts 02115*²*Laboratoire de Physique de la Matière Condensée, CNRS UMR No. 7643, Ecole Polytechnique, 91128 Palaiseau, France*

(Received 3 December 2001; revised manuscript received 9 July 2002; published 30 December 2002)

Eutectic two-phase cells, also known as eutectic colonies, are commonly observed during the solidification of ternary alloys when the composition is close to a binary eutectic valley. In analogy with the solidification cells formed in dilute binary alloys, colony formation is triggered by a morphological instability of a macroscopically planar eutectic solidification front due to the rejection by both solid phases of a ternary impurity that diffuses in the liquid. Here we develop a phase-field model of a binary eutectic with a dilute ternary impurity. We investigate by dynamical simulations both the initial linear regime of this instability, and the subsequent highly nonlinear evolution of the interface that leads to fully developed two-phase cells with a spacing much larger than the lamellar spacing. We find a good overall agreement with our recent linear stability analysis [M. Plapp and A. Karma, *Phys. Rev. E* **60**, 6865 (1999)], which predicts a destabilization of the front by long-wavelength modes that may be stationary or oscillatory. A fine comparison, however, reveals that the assumption commonly attributed to Cahn that lamellae grow perpendicular to the envelope of the solidification front is weakly violated in the phase-field simulations. We show that, even though weak, this violation has an important quantitative effect on the stability properties of the eutectic front. We also investigate the dynamics of fully developed colonies and find that the large-scale envelope of the composite eutectic front does not converge to a steady state, but exhibits cell elimination and tip-splitting events up to the largest times simulated.

DOI: 10.1103/PhysRevE.66.061608

PACS number(s): 68.70.+w, 81.30.-t, 02.60.Cb

I. INTRODUCTION

Eutectic alloys can form a wealth of different two-phase patterns during solidification. These alloys are of interest to metallurgists [1] because of their low melting points and of the superior mechanical properties associated with a fine-scale composite microstructure. Moreover, eutectic growth is a nontrivial example of pattern formation outside of equilibrium that has attracted the attention of physicists over the last two decades.

When the two solid phases (α and β) of a binary eutectic alloy have rough interfaces with the liquid, solidification at or near the eutectic composition typically produces a spatially periodic array structure consisting of lamellar plates of the two phases, or of rods of the phase with the smaller volume fraction embedded inside the matrix of the other phase. Since the pioneering mathematical analyses by Hillert [2] and Jackson and Hunt [3], which built on earlier work by Brandt [4] and Zener [5], it is well established that these lamellar and rod morphologies can grow cooperatively in steady state for a continuous range of eutectic spacings, with both phases helping each other to grow via the diffusive transport of the two chemical components in the liquid (coupled growth).

In directional solidification experiments, a sample containing the alloy is pulled at a constant velocity v_p in an externally imposed temperature gradient of magnitude G . In such experiments, coupled growth typically produces a composite front that is perpendicular to the temperature gradient, and planar on a scale much larger than the lamellar spacing λ (defined as the width of the basic spatially repeating unit consisting of one α lamella and one β lamella). Analytical

[6] and numerical [7] studies of the morphological stability of lamellar eutectics, as well as detailed experiments in a transparent organic system [8], have shown that the stable range of lamellar spacings is restricted by a long-wavelength instability leading to local lamellar termination at small λ , and short-wavelength oscillatory instabilities at large λ . These studies clearly demonstrate that a large-scale morphological instability of the composite front does not occur in a binary eutectic alloy.

This picture is consistent with the experimental observation that such a morphological instability occurs only when a small quantity of a ternary impurity is present, and when v_p exceeds a critical value [9–19]. In a nonlinear regime, this instability results in the formation of two-phase solidification cells, also called eutectic colonies, with a typical width much larger than λ . A typical example of such cells is shown in Fig. 1.

Experimental measurements to date [9–19] have consistently shown that the onset of colony formation can be relatively well described by a simple constitutional supercooling

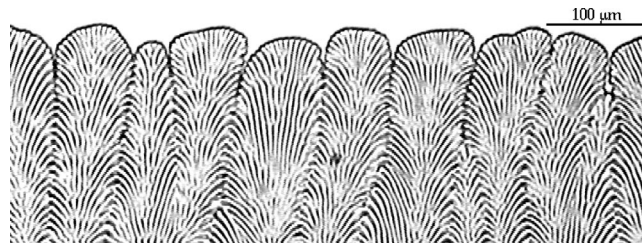


FIG. 1. Eutectic colonies in a thin sample of the transparent organic eutectic alloy $\text{CBr}_4\text{-C}_2\text{Cl}_6$, doped with a small amount of the ternary impurity naphthalene (from Ref. [18]).

criterion with respect to the ternary impurity [20,21], which predicts that the instability occurs when G/v_p falls below a critical value. This suggests that this instability may be qualitatively similar to the well-known Mullins-Sekerka instability of a monophasic front during directional solidification of a dilute binary alloy [22]. In a recent linear stability analysis of a sharp interface model [23], however, we showed that the morphological instability of a composite front in the presence of a dilute ternary impurity differs fundamentally from the instability of a monophasic front, even though the onset of both instabilities is well predicted by constitutional supercooling. This analysis was based on the same procedure used previously by Datye and Langer [6] to analyze the stability of binary lamellar eutectics, where the basic degrees of freedom are the coordinates of the α - β -liquid trijunctions. Our main finding was that the amplification of linear perturbations of the composite front can be either steady or oscillatory for experimentally relevant control parameters, in contrast to the classical Mullins-Sekerka instability where finite-wavelength perturbations are amplified in a nonoscillatory way.

Furthermore, in Ref. [23], we developed an “effective monophasic front” formulation of the dynamics of the composite interface that shed light on the origin of this difference. We showed that the long-wavelength dynamics of the envelope of the composite front is governed by a free-boundary problem with boundary conditions for the concentration of the diffusing ternary impurity on the effective front that can be obtained by averaging over the properties of the two solid phases. As a self-consistency check, we also showed that, when the wavelength of the perturbation is much larger than λ , the linear stability analysis of this free-boundary problem gives identical results to the full stability calculation expressed in terms of the trijunction coordinates.

Not surprisingly, this free-boundary problem turns out to be very similar to the one governing a “true” monophasic front in a dilute binary alloy. The nontrivial difference, however, is that the local lamellar spacing, which appears in the boundary condition for the ternary impurity on the front, constitutes an additional “internal degree of freedom” of the front that modifies its stability properties, and gives rise to the oscillatory modes. Physically, this reflects the fact that the local temperature of the front depends on the local lamellar spacing λ and that, in turn, the time rate of change of λ depends on the shape of the front because of the geometrical constraints imposed by the equilibrium conditions for the angles between interfaces at the trijunctions (Young’s conditions).

In a recent experimental study of a transparent organic model alloy, oscillatory patterns compatible with the results of our linear stability analysis were indeed observed [18]. The same study, however, also revealed a wealth of other possible structures that can be associated with the instability of a planar front, and, in particular, localized two-phase fingers that may appear in an early stage of the morphological instability.

The two main goals of the present study are to check the validity of our previous linear stability analysis [23] by direct simulation of the fundamental equations of motion, and to

investigate the nonlinear regime of colony formation. For this purpose, we develop a phase-field model for the directional solidification of a eutectic alloy with a dilute ternary impurity. Simulations of this model enable us to characterize quantitatively the amplification and decay of linear perturbations of the composite front and to study the complex interface dynamics leading to the formation of well-developed colonies.

The phase-field method is by now a well-established technique for simulating solidification patterns [24–29]. In particular, it has already been applied to the investigation of multiphase solidification in eutectic and peritectic alloys [30–35]. The advantage of this method with respect to the boundary integral formalism used previously to perform detailed simulations of eutectic growth structures [7] is that ternary impurities can easily be included. Furthermore, the phase-field method is able to handle automatically dramatic changes in the interface morphology such as lamella termination and creation, which are difficult to implement in the boundary integral approach.

The phase-field model presented in this paper is specifically designed for computational efficiency and therefore makes some simplifying assumptions. In particular, we use a generic eutectic phase diagram that is symmetric with respect to the exchange of the two solid phases, and we neglect crystallographic effects such as the anisotropy of the solid-liquid and solid-solid interfacial energies. The computational effort required to simulate fully developed colonies is nonetheless considerable since the two-phase cell spacing is one order of magnitude larger than λ . For this reason, the largest simulations of such structures were carried out on a multi-processor CRAY T3E and took the equivalent of a few thousand hours of single-processor workstation time.

The simulation results are found to be in good overall agreement with our sharp-interface linear stability analysis for compositions close to the eutectic point, where the two solid phases have approximately equal volume fractions. We observe, indeed, the predicted large-scale oscillatory structures. Quantitatively, however, the simulated growth rates differ from the predicted ones. A careful analysis of our simulation results, extrapolated to the limit of vanishing thickness of the diffuse interfaces, allows us to pinpoint the origin of this discrepancy. In particular, our stability analysis uses the assumption that the lamellae grow normal to the large-scale growth front. This assumption is commonly attributed to Cahn and was also used previously by Datye and Langer [6] for their linear stability analysis of lamellar eutectics in binary alloys. We find that, in our simulations, this rule is slightly violated. Hence, the stability analysis correctly describes all the qualitative features of the instability, but would have to be extended to include this effect in order to become quantitatively accurate. This violation also has important consequences for the stability of binary eutectics that are discussed elsewhere [36].

The linear instability of the planar front is followed by a nonlinear transient that leads to the formation of fully developed colonies. The nature of the transient depends on the composition. In simulations carried out at the eutectic point, the long-wavelength modes grow until the front becomes

wavy and the first lamella terminations occur in the concave parts. Subsequently, the grooves deepen and the tips grow ahead of the front, such that the initial wavelength of the colonies corresponds to the linear mode that dominates the stability spectrum. In contrast, for off-eutectic compositions, the linear regime is much shorter, and localized two-phase fingers centered around a thin lamella of the minority phase grow rapidly ahead of the front and develop into colonies later on.

Finally, once formed, the colonies have a quite well-defined average size and shape at both eutectic and off-eutectic compositions. However, the front does not settle down into a true steady state, but exhibits tip-splitting and cell elimination events, not unlike the monophasic front of a dilute alloy in the absence of interfacial anisotropy [37,38].

The remainder of this paper is organized as follows. In the following section, we introduce the phase-field model and analyze its sharp-interface limit. In Sec. III, we present simulation results for stable steady-state lamellar growth that are used to test our model. Section IV contains a brief review of our sharp-interface linear stability analysis [23], and a detailed comparison between the analytical and numerical results concerning the linear stability of the eutectic front. Section V is devoted to the simulations of well-developed colony structures in a nonlinear regime. Finally, conclusions and an outlook for future work are given in Sec. VI.

II. PHASE-FIELD MODEL

We consider directional solidification of thin samples, as used in many experimental studies of pattern formation during solidification [8,12,18]. This allows us to treat the problem as essentially two-dimensional and to neglect convection in the liquid. Furthermore, we assume that the rejection of latent heat during solidification does not appreciably modify the temperature field created by the experimental setup (frozen temperature approximation), and hence that growth is limited by diffusion of the chemical constituents.

We are interested in the behavior of a ternary alloy close to a binary eutectic trough in the phase diagram. Specifically, we will consider a very low concentration of the third component, which can then be regarded as a dilute impurity. This allows us to neglect various cross-coupling terms between the ternary impurity and the components of the binary eutectic. In addition, we are more interested in generic aspects of two-phase cell formation than in modeling a specific material. Hence, we study a model eutectic alloy that has a symmetric phase diagram. This simplifies the setup of the phase-field model.

The principles of the phase-field method have been described in detail in numerous publications [24–35]. The idea is to distinguish between the different thermodynamic phases with the help of one or several scalar fields, the phase fields, that have fixed values in the bulk phases and vary continuously across smooth and diffuse interfaces. A free energy functional suitable for the problem at hand is then constructed, and the equations of motion for the fields are written in variational form. By now, various phase-field models for alloy solidification are available [27,29–35]. In particu-

lar, much effort was spent to develop a thermodynamically consistent approach and to base the free energy functional on ideal or regular solution models [27,32,34]. In contrast, we are interested here mainly in the phase-field model as a computational tool. We will therefore use a strongly simplified model that is chosen for its computational efficiency, with the minimum of ingredients necessary to reproduce the main features of eutectic solidification with a ternary impurity. The parameters of the model are related to physical quantities by performing a sharp-interface limit.

We choose as the set of dynamical field variables the concentration (in molar fraction) $c(x, z, t)$ of one of the components of the binary eutectic, the concentration $\tilde{c}(x, z, t)$ of impurities, and a single phase field $\phi(x, z, t)$ that distinguishes between solid and liquid. To simplify the construction of the free energy functional, we define the scaled concentration u by

$$u(x, z, t) = \frac{c(x, z, t) - c_E}{(c_\beta - c_\alpha)/2}, \quad (1)$$

where c_E , c_α , and c_β are the compositions of the liquid and the two solid phases in the pure binary eutectic at the eutectic temperature T_E [39]. For a symmetric phase diagram, the scaled compositions of the two solids at T_E are $u = \pm 1$.

Building on a previous phase-field model for a binary eutectic [30], we take the (dimensionless) free energy functional [40] of the form

$$F = \int_V dV \left[\frac{W_u^2}{2} (\nabla u)^2 + \frac{W_\phi^2}{2} (\nabla \phi)^2 + f(\phi, u, \tilde{c}, T) \right], \quad (2)$$

where V is the volume of the two-phase system. The dimensionless free energy density $f(\phi, u, \tilde{c}, T)$ must have three local minima to account for the three possible phases (liquid, α solid, and β solid), separated by potential barriers. We use the phase field to distinguish between solid and liquid, and the scaled concentration field to distinguish between the two solids. The gradient terms force the fields to vary continuously between the bulk equilibrium values and hence create interfaces of a characteristic thickness of order W_u (solid-solid interface) and W_ϕ (solid-liquid interfaces). In general, there should also be a gradient term for the ternary impurity. However, we may omit this term for simplicity since \tilde{c} has no indicator function, but is slaved to the other fields; that is, for specified phase field ϕ , concentration u and temperature T , the equilibrium value of \tilde{c} is known.

A convenient choice for the free energy density is

$$f(\phi, u, \tilde{c}, T) = -\frac{\phi^2}{4} + \frac{\phi^4}{8} + \frac{1+h(\phi)}{2} f_{\text{sol}}(u, \tilde{c}, T) + \frac{1-h(\phi)}{2} f_{\text{liq}}(u, \tilde{c}, T). \quad (3)$$

Here, f_{sol} and f_{liq} are the bulk free energy densities in the solid and the liquid, respectively, and

$$h(\phi) = \frac{3}{2} \left(\phi - \frac{\phi^3}{3} \right) \quad (4)$$

is an interpolation function. The first two terms in Eq. (3) generate a double well potential for ϕ with minima at $\phi = \pm 1$. Since $h(\pm 1) = \pm 1$, $f(1, u, \bar{c}, T) = f_{\text{sol}}(u, \bar{c}, T)$ and $f(-1, u, \bar{c}, T) = f_{\text{liq}}(u, \bar{c}, T)$, such that $\phi = +1$ corresponds to the solid and $\phi = -1$ to the liquid. Moreover, since $h'(\pm 1) = 0$, the equilibrium values of ϕ , given by the solutions of $df/d\phi = 0$, always remain at $\phi = \pm 1$, independently of the values of f_{sol} and f_{liq} . The expressions for f_{sol} and f_{liq} are given in the Appendix.

The equations of motion for the three fields are

$$\tau \partial_t \phi(x, z, t) = - \frac{\delta F}{\delta \phi(x, z, t)}, \quad (5)$$

$$\partial_t u(x, z, t) = \nabla \left(M(\phi, u, \bar{c}) \nabla \frac{\delta F}{\delta u(x, z, t)} \right), \quad (6)$$

$$\partial_t \bar{c}(x, z, t) = \nabla \left(\tilde{M}(\phi, u, \bar{c}) \nabla \frac{\delta F}{\delta \bar{c}(x, z, t)} \right), \quad (7)$$

where $\delta F / \delta(\cdot)$ denotes the functional derivative with respect to the field (\cdot) , τ is a (microscopic) relaxation time, and M and \tilde{M} are the mobilities of the eutectic component and the ternary impurity, respectively. These variational forms reflect the fact that the two concentrations are conserved fields, whereas the phase field can be seen as a nonconserved order parameter. The nonconserved phase field simply relaxes toward its local equilibrium value. Indeed, by inserting Eq. (3) into Eq. (5) we obtain

$$\tau \partial_t \phi = W_\phi^2 \nabla^2 \phi + \phi/2 - \phi^3/2 + h'(\phi)(f_{\text{liq}} - f_{\text{sol}}). \quad (8)$$

The last term on the right-hand side always drives the phase field to the value that corresponds to the lower local free energy density (we recall that $h' > 0$ and that $\phi = 1$ corresponds to the solid).

The definition of the model is completed by the specification of the mobility functions $M(\phi, u, \bar{c})$ and $\tilde{M}(\phi, u, \bar{c})$. The dependence of M and \tilde{M} on the phase field and the compositions allows us to obtain the desired diffusivities in the bulk phases. We want to simulate a one-sided model (i.e., vanishing diffusivity in the solid) with constant diffusivities for eutectic components and impurities in the liquid. This can be achieved by choosing

$$M(\phi, u, \bar{c}) = D \left[1 - \left(\frac{1 + \phi}{2} \right)^n \right], \quad (9a)$$

$$\tilde{M}(\phi, u, \bar{c}) = \tilde{D} \left[1 - \left(\frac{1 + \phi}{2} \right)^n \right] \bar{c}, \quad (9b)$$

where D and \tilde{D} are the diffusion constants. Indeed, from the equations of motion, we get that in the liquid ($\phi \equiv -1$)

$$\partial_t u = \nabla \left[M \left(\frac{\partial^2 f_{\text{liq}}}{\partial u^2} \nabla u + W_u^2 \nabla (\nabla^2 u) \right) \right], \quad (10)$$

$$\partial_t \bar{c} = \nabla \left(\tilde{M} \frac{\partial^2 f_{\text{liq}}}{\partial \bar{c}^2} \nabla \bar{c} \right). \quad (11)$$

In the first equation, we can neglect the term $W_u^2 \nabla (\nabla^2 u)$ in the brackets on the right-hand side, since the diffusion pattern forms on a scale much larger than W_u , and hence this term is small compared to $(\partial^2 f_{\text{liq}} / \partial c^2) \nabla u$. Using the expressions for the mobilities and f_{liq} , we obtain the desired result in the liquid,

$$\partial_t u = D \nabla^2 u, \quad (12)$$

$$\partial_t \bar{c} = \tilde{D} \nabla^2 \bar{c}. \quad (13)$$

The exponent n in the mobility plays a role only in the interfacial region where the phase field varies, and changing its value modifies the interface kinetics. This will be addressed in more detail below. The relation of the phase-field equations to the classic free-boundary formulation of solidification is discussed in the Appendix.

III. LAMELLAR STEADY STATES

We chose as a testing ground for our model the simulation of lamellar steady-state solutions. This has the additional benefit of providing us with the initial configurations needed for the simulations of large-scale arrays described below. In the laboratory frame, the sample is pulled with velocity v_p in a constant temperature gradient G along the z axis. This means that in the sample frame, the isotherms move toward the positive z direction with velocity v_p . Consequently, the temperature at a given point (x, z) of the sample is

$$T(z, t) = T_E + Gz - v_p t, \quad (14)$$

where we have chosen the origin of the z axis at the eutectic isotherm for $t = 0$.

The equations of motion were simulated by an explicit Euler algorithm with time step Δt on a simple square grid of spacing Δx using standard finite-difference formulas. For simplicity, we chose $W_u = W_\phi \equiv W$. In the following, unless otherwise stated, lengths will be measured in units of W , time in units of τ , and temperatures in units of T_E . We chose (see the Appendix for the definitions of the parameters) $D = \tilde{D} = 1$, $\alpha = 1$, $a = 1/8$ (parallel eutectic solidus and liquidus lines), $G = 0.001$, v_p between 0.005 and 0.02, and various values of b and K , with $\epsilon_l = 0$ and $\epsilon_s = -b \ln K$. Since the equation for the composition u is of fourth order, the critical time step for the occurrence of numerical instabilities scales as Δx^4 . The allowed grid spacing Δx , however, is limited by the requirement that the smooth interfaces be sufficiently well resolved to avoid strong numerical anisotropies and lattice pinning. We found that $\Delta x = 1$ and $\Delta t = 0.025$ provided a good compromise between efficiency and accuracy.

The simulations were started with a single pair of flat lamellae in contact with the liquid in a box of lateral size λ . The concentrations were set to the equilibrium values in each phase. For the subsequent evolution, periodic boundary conditions were used in the direction parallel to the isotherms, while the concentrations in the liquid were kept at fixed values u_∞ and \tilde{c}_∞ at the upper end of the simulation box. At the lower (solid) end, no boundary conditions are needed since the fields do not evolve. During the runs, the simulation box was periodically shifted to follow the interface. Convergence to the steady-state solution was checked by computing the average change of the phase field in the moving frame during the advance of the isotherms by one lattice spacing. Furthermore, the interface shapes (given by the level set $\phi=0$ for the solid-liquid interface and by $u=0$ in the solid, that is for $\phi>0$, for the solid-solid interfaces) are extracted by interpolation of the fields between the lattice points. This procedure yields a resolution far superior to the grid spacing. The average undercooling of the interface is then

$$\Delta T(t) = T_E - T_{int}(t) = -G \left(\frac{1}{\lambda} \int_0^\lambda \zeta(x,t) dx - v_p t \right), \quad (15)$$

where $\zeta(x,t)$ is the z position of the extracted solid-liquid interface as a function of x at time t . The simulations were stopped when the undercooling was to within 10^{-4} of its extrapolated final value.

We first discuss the special case of a pure (binary) eutectic at the eutectic composition, $u_\infty = \tilde{c}_\infty = 0$ (note that we omit the impurity terms in the free energy and the equation of motion for the impurities when $\tilde{c}_\infty = 0$). For our symmetric phase diagram, there is no global diffusion boundary layer in this case, and the diffusion field in the liquid decays exponentially on a scale of λ . Hence, a box length parallel to the temperature gradient of about five times λ was sufficient to obtain results that are independent of the box size. The interface relaxes exponentially to its steady state, with relaxation times of order λ^2/D ; on a typical modern workstation, the convergence takes a few hours.

In contrast, for $u_\infty \neq 0$ and/or $\tilde{c}_\infty \neq 0$, solute redistribution leads to a boundary layer of thickness $l_D = D/v_p$, much larger than λ . Its buildup takes a time of the order $D/(Kv_p^2)$, much larger than λ^2/D . Therefore, larger box sizes (of several times l_D along the growth direction) and longer simulation times have to be used. As a consequence, the convergence of a run takes several days of CPU time. Instead of relaxing exponentially as observed without boundary layer, the interface position follows a damped oscillation with exponential envelope. This is in agreement with the time-dependent analysis of solute redistribution by Warren and Langer [41].

Let us compare our results to the well-known Jackson-Hunt (JH) relation between lamellar spacing and interface undercooling [3], generalized to include the effect of the ternary impurities,

$$\Delta T(\lambda) = \Delta T_{JH}(\lambda) + \tilde{m} \tilde{c}_\infty / K, \quad (16)$$

$$\Delta T_{JH} = \frac{1}{2} \Delta T_{\min} \left(\frac{\lambda}{\lambda_{\min}} + \frac{\lambda_{\min}}{\lambda} \right). \quad (17)$$

The curve ΔT versus λ exhibits a minimum at a spacing λ_{\min} , where

$$\Delta T_{\min} = \frac{2m_u \Delta u}{\eta(1-\eta)} \sqrt{\frac{\Gamma \sin \theta P(\eta) v_p}{2Dm_u \Delta u}}, \quad (18)$$

$$\lambda_{\min} = \sqrt{\frac{2\Gamma \sin \theta D}{m_u \Delta u v_p P(\eta)}}. \quad (19)$$

Here, $\Delta u = u_\beta - u_\alpha = 2$ is the concentration difference between the two solids at the eutectic temperature, $\eta = (u_\beta - u_\infty)/\Delta u$ is the volume fraction of α phase in the solid, m_u is the liquidus slope in the binary eutectic phase diagram (defined in the Appendix), $P(\eta) = \sum_{n=1}^{\infty} \sin^2(\pi n \eta) / (\pi n)^3$, Γ is the Gibbs-Thomson coefficient, and θ is the contact angle defined by Eq. (A18) below. For $W_u = W_\phi = 1$, we obtain numerically $\gamma_{sl} = 1.04$, which together with $\gamma_{ss} = 2/3$ gives $\theta \approx 19^\circ$. Note that Eqs. (18) and (19) are valid only for our choice of a symmetric phase diagram; see Ref. [23] for a discussion of the general case. It should be kept in mind that the JH theory is approximate since it uses a flat interface to calculate the diffusion field. Nevertheless, it has been shown by boundary integral simulations [7] that the error is small for small contact angles θ and close to the spacing λ_{\min} , such that it can be used as a semiquantitative test for our phase-field model.

We computed the interface undercooling in our model for various pulling speeds and two different values of the mobility exponent n in Eqs. (9) of the mobility functions. Let us first discuss the results for $n=1$, which corresponds to the simplest form of the mobility that has been widely used before. The simulated undercoolings are slightly higher than the JH prediction, but the overall shape of the curve is perfectly reproduced. The difference can be attributed to the nonequilibrium effects (interface kinetics, solute trapping) present in the phase-field model, but neglected in the JH theory. Indeed, the differences between our simulations and the JH prediction are larger for higher v_p . Furthermore, we obtained λ_{\min} and ΔT_{\min} by fitting our simulation results to Eq. (17) and found that the scaling relation $\lambda_{\min}^2 v_p = \text{const}$ that can be derived from Eq. (19) is well satisfied. Regarding the impurity contribution to Eq. (16), we conducted simulations for various impurity concentrations, impurity liquidus slopes, and partition coefficients and found good agreement with the predicted behavior. In particular, we verified that the spacing λ_{\min} was not appreciably modified by the addition of impurities.

The range of lamellar spacings that can be simulated is limited by two effects that are intrinsic to our model. For spacings smaller than $\sim 16W$ ($\sim 8W$ for each individual lamella), the diffuse interfaces at the two sides of a lamella start to overlap, which leads to strong corrections to the sharp-interface limit and ultimately to lamella elimination.

For too large spacings, in turn, new lamellae of the opposite phase nucleate in the centers of the initial lamellae, leading to a lamellar array with one third of the initial spacing.

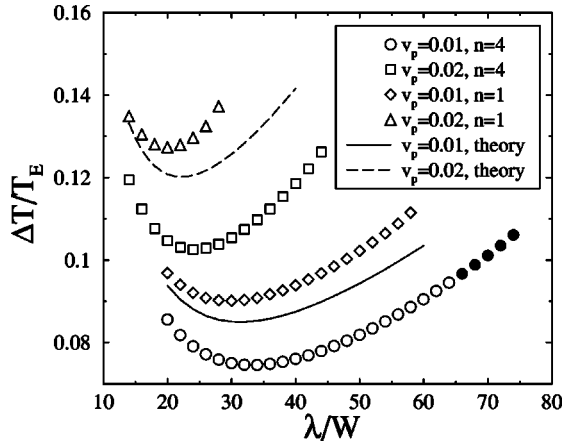


FIG. 2. Average interfacial undercooling versus lamellar spacing for several values of the pulling speed v_p and the mobility exponent n . Lines, prediction of the Jackson-Hunt theory, Eq. (17); symbols, simulation results. Filled circles correspond to steady states that are unstable with respect to $1-\lambda$ oscillations.

This is the result of a “spinodal decomposition” that takes place in the interface. Indeed, the equation for the composition in the solid far from the interface is exactly the classical Cahn-Hilliard equation [42], which is known to exhibit phase separation without nucleation in a composition range where the free energy density has a negative curvature ($\partial^2 f_{\text{sol}}/\partial c^2 < 0$). Far inside the solid, this has no importance here because the mobility is zero and hence no dynamics takes place. Well within the liquid, there is no unstable concentration range since the liquid free energy has a single well structure. But in the diffuse interface, new domains may form when the concentration falls within the unstable range. According to the JH theory, the deviations of the concentration from the equilibrium value at the interface scale as Pe , where the Péclet number $\text{Pe} = \lambda/l_D = \lambda v_p/D$; hence, the maximum spacing λ_{max} that can be simulated before nucleation sets in increases as v_p decreases. Indeed, we find $\lambda_{\text{max}}/W \sim 28$ for $v_p = 0.02$ and $\lambda_{\text{max}}/W \sim 58$ for $v_p = 0.01$.

It seems useful at this point to comment on the implications of these limitations for the choice of the computational parameters for large-scale simulations. The range of initial lamellar spacings of interest for the present study ranges from λ_{min} to about $1.5\lambda_{\text{min}}$. Since we want to simulate the linear instability of a lamellar front, which may involve considerable variations of the local lamellar spacing, the model should work for a sizable range of spacings, say at least for spacings that are $\pm 50\%$ of the initial value. Therefore, we need a model that works for spacings between $\approx 0.5\lambda_{\text{min}}$ and $\approx 2.25\lambda_{\text{min}}$.

The first consequence is that we must have $\lambda_{\text{min}}/W > 32$ because of the low-spacing limitation. Next, λ_{min} should not be much larger than this value, since the computer time necessary to simulate the evolution of an array of initial spacing λ_{min} can be estimated to scale as λ_{min}^5 (number of grid points: $\lambda_{\text{min}} \times \lambda_{\text{min}}$; time for the interface to advance by one spacing: λ_{min}/v_p ; using $\lambda_{\text{min}}^2 v_p = \text{const}$, we get $t_{\text{CPU}} \sim \lambda_{\text{min}}^5 \sim v_p^{-5/2}$). From Fig. 2, we can see that $n = 1$ and $v_p = 0.01$ give λ_{min} of the right order of magnitude; however, since $\lambda_{\text{max}}/W \sim 58$,

the available range of lamellar spacings is somewhat small (for an initial spacing of $1.5\lambda_{\text{min}}$, nucleation would set in for an increase of the local spacing by only 30%). Since the range of available spacings increases with decreasing pulling speed, one possible solution would be to further reduce v_p . However, as discussed above, the necessary computer time rapidly becomes prohibitive.

Another way out is to change the exponent in the equations for the mobilities, Eqs. (9). If we choose $n > 1$, the diffusivity is increased in the whole interfacial region, whereas it remains zero in the solid. This leads to higher diffusion currents along the surface than for $n = 1$. Hence, the pileup of the rejected atoms at the interface is lower, and consequently λ_{max} is higher. The price to pay is that this model, in its sharp-interface limit, is not equivalent to the classical JH model, but contains additional surface diffusion terms [43]. However, as shown in Fig. 2, the qualitative behavior of the undercooling versus spacing curve does not change. For $v_p = 0.01$, λ_{min} is larger than the theoretical JH value by about 10%, whereas ΔT_{min} is about 15% too low. On the other hand, $\lambda_{\text{max}}/W = 74$, such that we now have at our disposal a sufficient range of spacings.

For these parameters, we observe for large spacings the well-known period-preserving oscillatory instability that sets in at about $2\lambda_{\text{min}}$ [7]. Even beyond the threshold of this instability, steady states can be reached to within an excellent precision, because we start from an exactly symmetric initial condition and because the numerical noise of the phase-field approach is extremely low. To trigger the instability within a reasonable simulation time, an explicit perturbation that breaks the symmetry between the two phases had to be added. Such unstable steady states are shown as filled symbols in Fig. 2.

The mechanism for lamella creation by nucleation is in fact very useful for the simulations of well-developed colonies where lamellae are frequently created at the solidification front. We want to confront our simulations with the experimental findings of Akamatsu and Faivre [18], who work with thin samples of a transparent eutectic alloy enclosed between parallel glass plates. In their experiments, creation of new lamellae indeed takes place predominantly in the center of already existing lamellae. However, the detailed mechanism is still unknown. New lamella do not form by nucleation, since the interfacial undercoolings are not high enough. Most likely, the “pockets” in the center of large lamellae are “invaded” from preexisting neighboring lamellae of the opposite solid by fingers that grow in the meniscus between the glass plates and the growing solid. The point here is that the modeling of such a process is out of reach for our present computational resources, since it is necessarily three-dimensional. Within the framework of two-dimensional simulations, we simply need a criterion to decide when new lamella should form, and the “automatic” implementation of a maximal lamellar width λ_{max} in our model is an adequate solution that avoids the implementation of an explicit nucleation rule, as done, for example, in Ref. [35].

The last question to settle, then, is how to choose λ_{max} for the simulations of well-developed colonies. For this, we need to anticipate how the choice of this quantity influences the

outcome of the simulations. As will be detailed below, the variation of undercooling with spacing is an important ingredient of the pattern formation process; therefore, we again need a sizable range of lamellar spacings around λ_{\min} . However, λ_{\max} must not be too large either. As mentioned above, the well-known short-wavelength instabilities appear for $\lambda > 2\lambda_{\min}$. In the experiments of Ref. [18], such oscillatory structures are seen occasionally in the center of flat colonies before the creation of new lamellae. This indicates that lamellae creation occurs at spacings only slightly larger than $2\lambda_{\min}$. Therefore, $n=4$ and $v_p=0.01$ with $\lambda_{\max}/\lambda_{\min}\approx 2.2$ is again a good choice. We did not carry out a systematic study to test the influence of λ_{\max} on the final colony patterns because this requires prohibitively long simulation times; however, due to the arguments outlined above, we expect the patterns to be fairly insensitive to this parameter as long as it stays between ≈ 1.5 to ≈ 2.5 times λ_{\min} .

IV. LINEAR STABILITY OF LAMELLAR ARRAYS

A. Theory

We have recently performed a detailed linear stability analysis of a lamellar eutectic interface in the presence of ternary impurities. Rather than repeating the calculations here, we will give a brief summary of the main assumptions and results before discussing the phase-field simulations. Our analysis is an extension of the method used by Datye and Langer to analyze the stability of lamellar arrays without impurities [6]. It is based on a perturbation scheme for the Jackson-Hunt solution and proceeds as follows.

(1) The coordinates of the trijunction points are chosen as fundamental variables to describe the state of the perturbed system. This amounts to a “discretization” of the original continuous system. Each trijunction point has two degrees of freedom, namely, its x and z positions (motion parallel and normal to the isotherms, respectively).

(2) For a lamellar interface that is gently curved on a scale much larger than λ , the lamellae are assumed to grow perpendicular to the envelope of the composite front (Cahn’s hypothesis). This connects the time derivative of the local lamellar spacing to the shape of the front. For example, in a protrusion where the front curves outward, the local spacing increases during further growth.

(3) Given the positions of the trijunction points, the actual interface shape is replaced by a piecewise planar interface, and a perturbed diffusion field is calculated. The Gibbs-Thomson equation is then used to obtain an eigenvalue problem for normal modes, i.e., perturbations proportional to $\exp(ikx + \omega t)$, where k is the wave number of the periodic perturbation, and ω its growth rate. The solutions of the eigenvalue equation give the dispersion relations $\omega(k)$. Since there are four degrees of freedom per lamella pair (two for each trijunction), $\omega(k)$ has four branches. Of those, there are two that are relevant for the long-wavelength instability we are interested in.

It turns out that the final result of this rather complicated analysis can be understood in terms of an effective front approach. Namely, one can separate two scales: the local

lamellar spacing, and the large-scale smooth envelope of the lamellar front. The evolution of the local spacing is slaved to the shape of the front by the assumption of normal motion (Cahn’s hypothesis). On the scale of the smooth front, the lamellar structure introduces an interfacial undercooling that is approximately given by the JH law, taken with the local spacing and interface velocity. Using these ingredients, it is possible to include the lamellar geometry in the usual Mullins-Sekerka stability analysis and to obtain the dispersion relation. This result can be recovered from the more complicated discrete analysis, with one additional ingredient. The eutectic diffusion field that governs the exchange of atoms between neighboring lamellae gives, when perturbed on a large scale, a stabilizing contribution to the total interfacial undercooling. The functional form of this stabilization is the same as for the surface tension terms, and this effect can therefore be included in the simple effective front approach by simply “renormalizing” the capillary length.

The two main results of this analysis are that (i) the instability threshold is close to the well-known constitutional supercooling criterion, with a small capillary correction, and (ii) in contrast to the Mullins-Sekerka instability, where unstable modes always have real growth rates, the lamellar structure may lead to complex growth rates, and hence to oscillatory modes. The origin of these oscillations can be understood as follows: in a protrusion of the front, the lamellar spacing increases. This leads to a local change in the JH undercooling that, for a small distortion of an array of spacing λ_0 , is proportional to the slope of the JH plot. For $\lambda_0 > \lambda_{\min}$, this provides a “restoring force” for the large-scale front. Since only the *change with time* of the lamellar spacing (but not the spacing itself) is related to the shape of the front, the dispersion relation becomes quadratic in ω , instead of the linear Mullins-Sekerka equation. There are two solutions to this equation for each wave number k . In physical terms, this is the consequence of the additional “internal degree of freedom” λ of the front. As discussed in detail in Ref. [23], real and complex growth rates may occur, depending on the ratio G/v_p , the lamellar spacing, and the impurity content. For large enough spacings, when the “restoring force” mentioned above is strong enough, we expect that the complete dispersion relation is complex. One of the goals of the present paper is to test this prediction by direct simulation of the basic equations of motion.

B. Single mode simulations

Let us first study the behavior of a single unstable mode of a lamellar array with initial spacing λ_0 . The parameters besides λ_0 that control stability are the impurity content and the ratio G/v_p . We define the dimensionless parameters

$$\Lambda = \lambda_0 / \lambda_{\min}, \quad (20)$$

$$w = \frac{\tilde{m}\Delta\tilde{c}}{m_u\Delta u} = \frac{\tilde{m}\tilde{c}_\infty(1/K-1)}{m\Delta c}, \quad (21)$$

$$g = \frac{2DG}{v_p m_u \Delta u} = \frac{2DG}{v_p m \Delta c}. \quad (22)$$

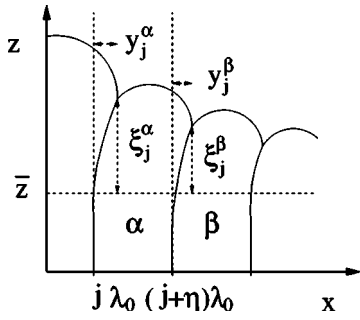


FIG. 3. Sketch of a perturbed lamellar interface that shows the definitions of the displacements ξ_j^α , ξ_j^β , y_j^α , and y_j^β .

Here, λ_{\min} is obtained from an interpolation of our simulation data shown in Fig. 2. For $n=4$ and $v_p=0.01$, $\lambda_{\min} \approx 34$. The freezing ranges of the eutectic and the impurities are, expressed in the parameters defined in the Appendix, $m_u \Delta u = 2T_E/\alpha$, and $\bar{m} \Delta \bar{c} = \bar{m}(1/K-1)\bar{c}_\infty = b(1-K)^2 T_E \bar{c}_\infty / (K\alpha)$.

A lamellar array is prepared by replicating the steady-state solution for one lamella pair N times. We apply a cosine perturbation to the steady state and impose the initial condition

$$\phi(x, z, 0) = \phi_0(x, z + A_0 \cos(2\pi x/N)), \quad (23)$$

where $\phi_0(x, z)$ is the steady-state solution. The other fields (u and \bar{c}) are perturbed in the same manner. The perturbation amplitudes A_0 are usually much smaller than the interface width (typically, $A_0/W < 0.1$), and the values on the grid points are obtained by linear interpolation of the numerical steady-state solution.

To analyze the evolution of the system, we store periodically the positions of all the interfaces (solid-solid and solid-liquid). In addition, we determine the positions of all the trijunction points by searching the intersections of the level curves $\phi=0$ and $u=0$. The coordinates of the trijunction point to the left of the ν lamella ($\nu = \alpha, \beta$) in the lamella pair number n are labeled (x_n^ν, z_n^ν) . We define the deviations of the trijunction point coordinates from their steady-state values (see Fig. 3),

$$\xi_n^\nu = z_n^\nu - \bar{z}, \quad (24a)$$

$$y_n^\nu = x_n^\nu - \bar{x}_n^\nu, \quad (24b)$$

where $\bar{x}_n^\alpha = n\lambda_0$ and $\bar{x}_n^\beta = (n + \eta)\lambda_0$, as well as their discrete Fourier transforms,

$$X_\nu(\kappa, t) = \frac{1}{N} \sum_{n=0}^{N-1} \xi_n^\nu \exp(2\pi i \kappa n), \quad (25)$$

$$Y_\nu(\kappa, t) = \frac{1}{N} \sum_{n=0}^{N-1} y_n^\nu \exp(2\pi i \kappa n), \quad (26)$$

where $\kappa = k\lambda_0/(2\pi)$ is a dimensionless wave number.

In Fig. 4, we show the evolution of an array of five lamellae, started in a single mode with $\kappa=0.2$. An oscillatory $5-\lambda$

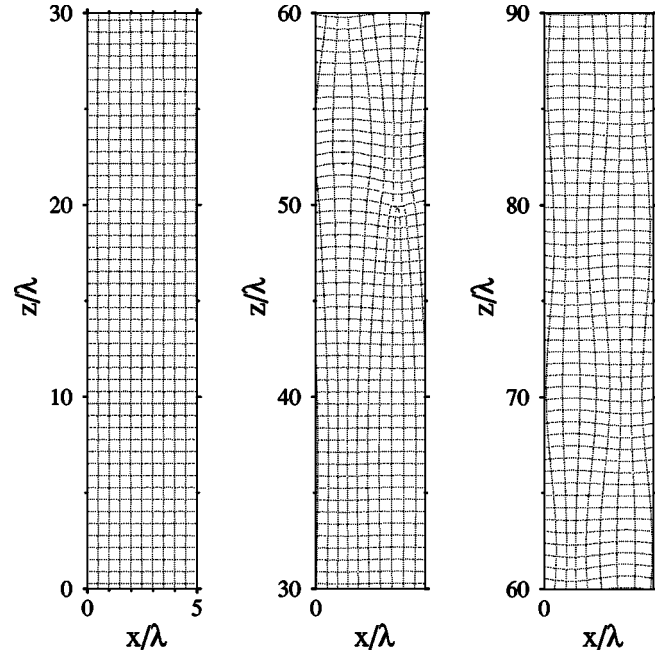


FIG. 4. Evolution of oscillatory modes. Growth direction is from bottom to top, and three successive frames are shown from left to right. Shown are the solid-solid interfaces, as well as successive snapshot pictures of the solid-liquid interfaces. The system is perturbed with a single cosine mode of dimensionless wave number $\kappa=0.2$. Simulation parameters: $v_p=0.01$, $G=0.0005$, $\lambda_0=40$, $K=0.5$, $\bar{c}_\infty=0.08$, $b=10$, giving $\Lambda=1.175$, $w=0.2$, $g=0.05$.

mode develops. Its amplitude grows until a lamella termination occurs at $z/\lambda_0=50$. Subsequently, the system shows a decaying $4-\lambda$ oscillation and approaches a steady-state solution with four lamella pairs. To analyze this evolution, we use the Fourier components $X_\nu(\kappa, t)$. Since the initial perturbation is not proportional to the (unknown) eigenvector corresponding to a single mode of the complete (continuous) system, the Fourier components for $\kappa \neq 0.2$ will not remain zero. However, they remain sufficiently small to be neglected in the data analysis. In Fig. 5, we show the evolution of

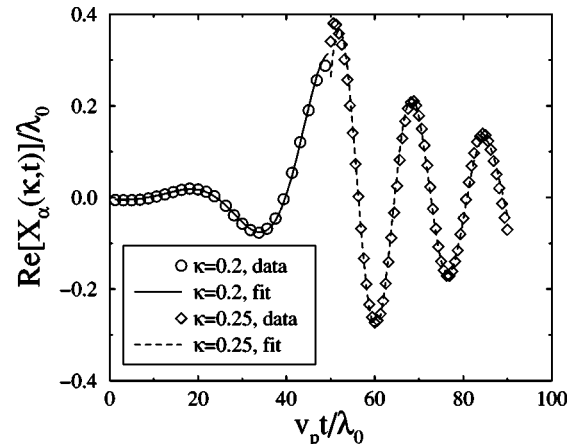


FIG. 5. Real part of the Fourier amplitude $X_\alpha(\kappa, t)$ as a function of time, for the run of Fig. 4. Also shown are the fits to growing (decaying) oscillating exponentials.

$\text{Re}[X_\alpha(\kappa, t)]$ versus time, for $\kappa=0.2$ before the lamella elimination, and for $\kappa=0.25$ afterwards (note that the elimination of one lamella pair corresponds to a change in the unperturbed lamellar spacing λ_0). Oscillating modes correspond to complex growth rates. We define the dimensionless growth rate by

$$\Omega = \omega \lambda_0 / v_p = \Omega_r + i\Omega_i, \quad (27)$$

with Ω_r and Ω_i real. The growth rate is determined by a fit of the data to the function

$$\text{Re}[X_\alpha(\kappa, t)] = A \exp(\Omega_r t) \sin[\Omega_i(t - t_0)], \quad (28)$$

where t is measured in units of λ_0 / v_p . In practice, we obtain a value of t_0 , i.e., the time of one of the zero crossings, by numerical interpolation, and then use a least-squares fitting procedure with A , Ω_r , and Ω_i as free parameters. As can be seen from Fig. 5, the fit is excellent. Surprisingly, the fit remains accurate up to the immediate vicinity of the lamella termination event. This indicates that the system is well described by a single, exponentially growing mode even for large deformations of the initial array. In particular, the linearization that is the basis for the theoretical analysis remains valid even if the lateral displacements are large, i.e., $y_i^v / \lambda_0 \sim 1$.

C. Dispersion relations

The simulation and fitting procedures outlined above were carried out for various values of the control parameters and arrays of different sizes to construct the dispersion relations $\Omega(\kappa)$. In Fig. 6, we show a comparison of the obtained data with the theoretical predictions of Ref. [23] for two different values of the temperature gradient. For both dispersion relations, there are stationary (Ω real) and oscillatory (Ω complex) modes. According to theory, for $g=0.05$ the fastest growing mode is stationary, whereas for $g=0.1$ it is oscillatory.

In all cases, the nature of the mode (stationary or oscillatory) agrees with the theoretical predictions. Furthermore, the oscillation frequency of the complex modes (Ω_i) is always in good quantitative agreement with theory. In contrast, the growth rates (Ω_r) are in good agreement only for small wave numbers; for large wave numbers, the simulated growth rates are systematically much smaller than predicted by theory, and the difference increases with the dimensionless wave number. Therefore, in the simulations at $g=0.1$, the fastest growing mode is stationary, and not complex as predicted by theory. For $\Lambda=1.47$ and $g=0.1$, we obtain a stability spectrum that is entirely complex (data not shown), both in theory and simulations.

Just as the JH theory, our stability analysis of a lamellar array contains several simplifying assumptions. It is therefore necessary to check whether the differences between theory and simulations are due to the approximations made in the stability analysis, or due to the phase-field approach, which is a genuine representation of the original free-boundary problem only in the limit $W/\lambda \rightarrow 0$. Therefore, we focused on a single complex mode at $g=0.1$ and $\kappa=0.2$

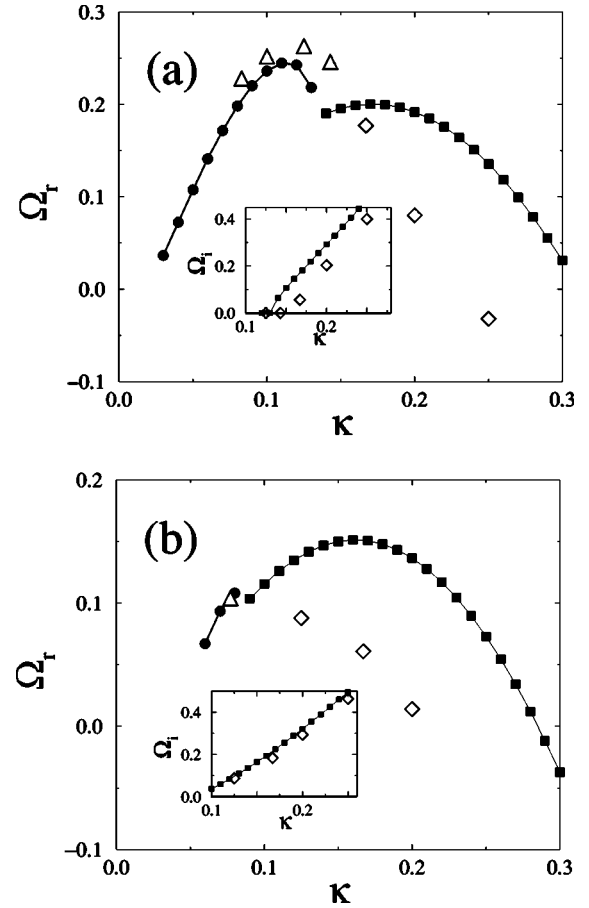


FIG. 6. Plots of the dimensionless growth rate Ω versus dimensionless wave number κ . The main graphs show the real part Ω_r , the insets the imaginary part Ω_i for (a) $\Lambda=1.175$, $w=0.2$, $g=0.05$ and (b) $\Lambda=1.175$, $w=0.2$, $g=0.1$. Filled symbols and lines, theoretical predictions from Ref. [23]; circles, real modes ($\Omega_i=0$); squares, complex modes ($\Omega_i \neq 0$). Open symbols, simulation data; triangles, real modes; diamonds, complex modes.

(5- λ oscillation) and conducted a series of runs with decreasing pulling speed v_p . Since $\lambda_{\min} \sim v_p^{-1/2}$, we increased the spacing λ_0 to keep the reduced spacing Λ constant. The temperature gradient G was also decreased to keep g constant.

The results for the growth rate Ω_r versus v_p are shown in Fig. 7. The data fall on a straight line, and by extrapolation to $v_p=0$ we find $\Omega_r(v_p=0)=0.085$. In contrast, the variation of the oscillation frequency is very small (from $\Omega_i=0.291$ at $v_p=0.01$ to $\Omega_i=0.302$ at $v_p=0.005$). This linear variation of Ω_r with v_p indicates that the dominant corrections to the sharp-interface limit of the phase-field model scale as $W/l_D = Wv_p/D$. Corrections in the other involved small ratios, W/λ_0 and λ_0/l_D , seem to be subdominant, since both scale as $1/\sqrt{v_p}$ at constant Λ . An example for a correction that scales as W/l_D is the interface kinetics; however, inserting a kinetic term in the Mullins-Sekerka analysis does not lead to a linear variation of the growth rate with the kinetic coefficient. The solute trapping effect also scales as W/l_D , but since it is quite involved to evaluate its influence on the growth rates, we have not investigated this issue in more

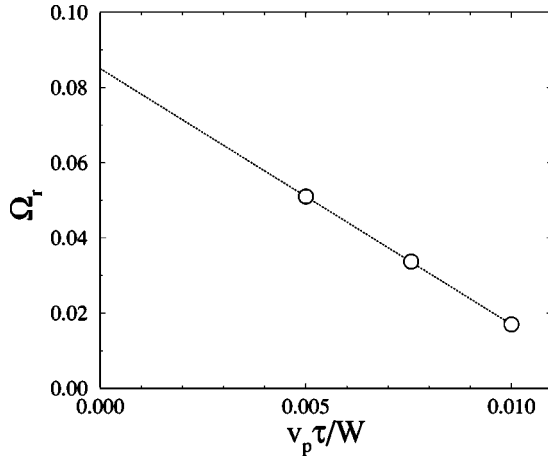


FIG. 7. Real part of the dimensionless growth rate Ω versus pulling speed for $\Lambda = 1.175$, $g = 0.1$, $w = 0.2$, and $\kappa = 0.2$. Symbols: simulation result. Dotted line: linear extrapolation to $v_p = 0$.

detail. We checked, however, that the variation of Ω_r with v_p is not a consequence of the surface diffusion term introduced by our choice $n=4$ in the mobility function: a simulation with $n=1$ and comparable Λ yielded similar results.

D. Test of Cahn's hypothesis

The simulated growth rate, extrapolated to $v_p = 0$, is still markedly different from the theoretical prediction $\Omega_r = 0.1365$. We therefore checked several assumptions that are used in the linear stability analysis, in particular, Cahn's hypothesis that the lamellae always grow perpendicular to the large-scale front. Expressed in terms of the trijunction point coordinates defined in Eq. (24) and Fig. 3, this assumption reads

$$\partial_t y_n^\beta = -\frac{v_p}{\lambda_0} (\xi_{n+1}^\alpha - \xi_n^\alpha) \quad (29)$$

for the trijunction point to the left of the n th β lamella. From the simulation data, explicit values of $\partial_t y_n^\beta$ and the vertical displacements ξ_n^α are available, and Eq. (29) can be directly checked.

In Fig. 8, we plot the measured $\partial_t y_n^\beta$ for one trijunction together with the prediction of Eq. (29). The two do not agree: Cahn's hypothesis is clearly violated. Most noticeably, there is a phase shift between the measured and the predicted curves. We found that the difference between the two curves is in phase with the lateral positions of the trijunction y_n^β . However, the coordinate itself cannot appear directly in an extension of Eq. (29), since the dynamics is invariant with respect to a global translation along the x direction. The simplest local expression that has the required translational invariance and is proportional to y_n^β is $y_{n+1}^\beta + y_{n-1}^\beta - 2y_n^\beta$. Therefore, we tried to fit the trijunction motion with the modified equation

$$\partial_t y_n^\beta = -\frac{v_p}{\lambda_0} (\xi_{n+1}^\alpha - \xi_n^\alpha) + \frac{v_p}{\lambda_0} B (y_{n+1}^\beta + y_{n-1}^\beta - 2y_n^\beta) \quad (30)$$

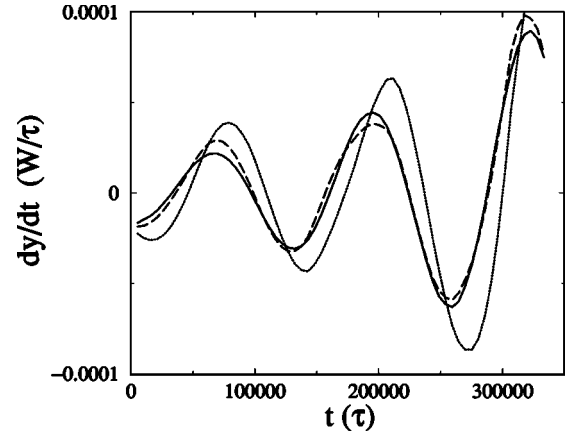


FIG. 8. Sideways velocity, dy/dt , of one trijunction point for $\Lambda = 1.175$, $g = 0.1$, $w = 0.2$, $\kappa = 0.2$, and $v_p = 0.00751$. Solid line: data extracted from the simulated curve $y(t)$. Dotted line: prediction of Cahn's hypothesis. Dashed line: best fit to Eq. (30).

that has a single adjustable parameter B . Note that the factor v_p/λ_0 has been included to make the parameter B a dimensionless number. As shown in Fig. 8, the resulting best fit is much closer to the real trijunction trajectory than Eq. (29).

Next, we repeated the above fit for all our simulation data. The results are shown in Fig. 9. Remarkably, the correction given by Eq. (30) works both for oscillatory and stationary modes, and the fit parameter B is independent of the wavelength. This shows that the violation of Cahn's hypothesis is a consequence of the local front geometry, and not a cooperative effect depending on the nature of the mode. The data for different temperature gradients g and partition coefficients K are statistically indistinguishable; the only parameter that has a marked influence on the fit parameter B is the spacing Λ .

To obtain more information about the coefficient B and its dependence on the control parameters, it is quite cumbersome to work with series of single mode runs as shown in Fig. 9. Therefore, we checked that the modified Eq. (30) also works for lamellar arrays that are started from a random

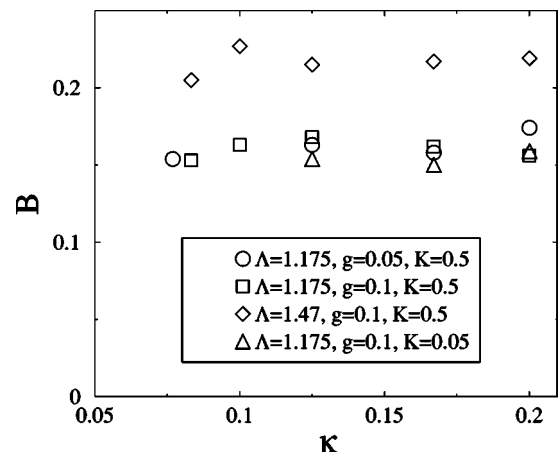


FIG. 9. Fit parameter B versus perturbation wave number κ for various sets of control parameters. The data include both oscillatory and stationary modes.

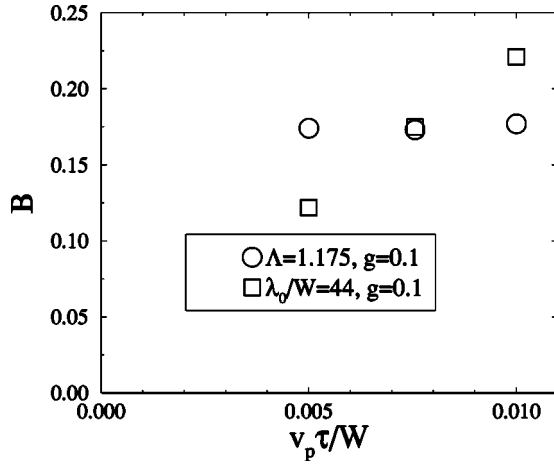


FIG. 10. Fit parameter B versus pulling speed v_p , for constant Λ ($\lambda_0 \sim v_p^{-1/2}$, circles) and for constant λ_0 ($\Lambda \sim v_p^{1/2}$, squares).

configuration, as will be described in more detail below. Furthermore, as can be guessed from the fact that B depends on the spacing Λ but not on the partition coefficient K or the impurity content, the new term is also present in eutectics without impurities. Hence, we performed simulations without impurities ($\tilde{c}_\infty = 0$) of arrays consisting of 20 lamellae pairs and obtained the parameter B from a simultaneous fit of all the trijunction trajectories with Eq. (30).

We found that B is almost independent of g over at least one decade in g : simulations at $\Lambda = 0.96$ and $g = 0.1, 0.2, 0.5,$ and 1 yielded $B = 0.135, 0.136, 0.140,$ and $0.141,$ respectively. The dependence of B on v_p was checked in two series of runs. The first series is the same as in Fig. 7: the velocity was decreased while g and Λ were kept constant. Remarkably, the values of B are independent of the velocity as is shown in Fig. 10. Therefore, B is independent of the ratios λ_0/W and W/l_D , and it can be concluded that the correction to Cahn's rule is not an artifact due to the finite interface width of the phase-field model. In the second series of runs, we decreased v_p while keeping λ_0 fixed; since λ_{\min} changes with v_p , this corresponds to a change in Λ . As can be seen in Fig. 10, now the coefficient B is no longer a constant. According to Eq. (30), this implies that, at fixed spacing λ_0 , the new contribution to the sideways velocity of the trijunctions is not simply proportional to the pulling speed. Finally, Fig. 11 shows the dependence of B on the reduced spacing Λ . All the data points for different temperature gradients and pulling speeds fall on a single curve that can be reasonably well approximated by the simple form

$$B \approx 0.15\Lambda. \quad (31)$$

To make the physical meaning of the parameter B more apparent, Eq. (30) can be rewritten in a slightly different form,

$$\partial_t y_n^\beta = -\frac{v_p}{\lambda_0}(\xi_{n+1}^\alpha - \xi_n^\alpha) + v_p \lambda_0 B \frac{y_{n+1}^\beta + y_{n-1}^\beta - 2y_n^\beta}{\lambda_0^2}. \quad (32)$$

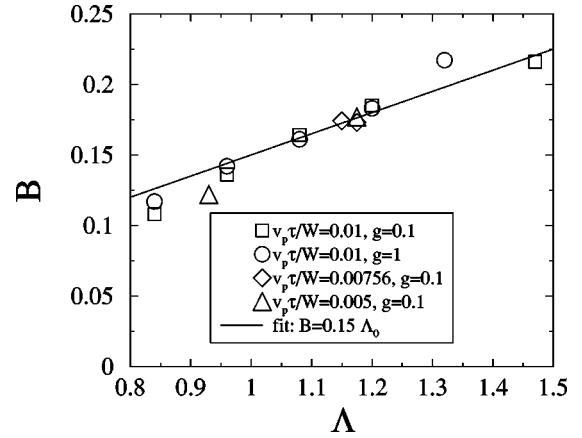


FIG. 11. Fit parameter B versus reduced spacing Λ .

The expression $(y_{n+1}^\beta + y_{n-1}^\beta - 2y_n^\beta)/\lambda_0^2$ on the right-hand side can be interpreted as a finite-difference approximation for the continuous second derivative $\partial_{xx}y$ of a smooth function $y(x)$ that interpolates between the lateral trijunction displacements. Since the product $v_p \lambda_0$ has the dimension of a diffusion coefficient, this term describes a lateral diffusion of the trijunctions. Furthermore, for $y(x)$ varying slowly on the scale of λ_0 , we have

$$\lambda(x) \sim \lambda_0(1 + \partial_x y), \quad (33)$$

such that the new contribution to the lateral trijunction speed is proportional to the gradient of the local spacing. The motion of the trijunctions is therefore a combination of the perpendicular lamellar growth according to Cahn's rule and a small lateral drift proportional to the gradient of the local spacing. Finally, by using again Eq. (33), one can easily show that the continuous version of Eq. (32) is equivalent to a diffusion equation for the local spacing $\lambda(x)$, the so-called phase-diffusion equation [44]. The new term constitutes therefore a positive contribution to the phase-diffusion coefficient, which makes immediately clear why it always has a stabilizing effect on the front. Putting together Eq. (31) and the prefactor $v_p \lambda_0$ in Eq. (32), we find that it scales as $v_p \lambda_0^2 / \lambda_{\min}$. One can also write this result in terms of the solute diffusion coefficient and dimensionless quantities as $D\Lambda Pe$ (we recall that the Péclet number $Pe = \lambda_0 / l_D$). We could not find any obvious simple argument that explains this scaling. The fact that the reduced spacing Λ appears in Eq. (31) indicates that the new term most likely arises from the interaction of the interlamellar diffusion field and the nonplanar front geometry on the scale of the individual lamellae.

Earlier theoretical studies of eutectic stability [45,46] have shown that there exist corrections to the purely "geometric" value of the phase-diffusion coefficient derived from Cahn's rule [44] in the limit of large thermal gradients ($g \gg 1$), when the front is almost flat. This is important for binary eutectics, because in the absence of an impurity-driven morphological instability, the long-wavelength stability of the front is controlled by the zero crossing of the phase-diffusion coefficient. It was shown that the smallest

possible eutectic spacing can become significantly smaller than λ_{\min} . The correction to Cahn's rule elucidated here also produces a similar deviation, but with the important difference that it is quantitatively significant even for the small thermal gradients used here ($0.1 < g < 1$), where the solid-liquid interfaces are round arcs connecting trijunctions. In this small g regime, the study of Chen and Davis [46] predicts a negligible shift of the small spacing stability limit of eutectic growth from λ_{\min} , and no comparison can be made with the study of Brattkus *et al.* [45] that is limited to the large g limit. We therefore conclude that these earlier studies do not capture the correction to Cahn's rule found here. The consequence of this new correction for the small spacing stability limit of eutectic growth in binary systems is explored in more detail in a recent paper that reports both phase-field simulations and experimental results [36].

Although Cahn's rule is violated, the resulting deviations of the growth angles from 90° are very small. To see this, let us use the geometrical relation $\partial_t y_n^\beta = -v_p \tan \delta_n^\beta$, where δ_n^β is the angle between the solid-solid interface at the trijunction and the z direction. From Eq. (30) we can calculate the deviation of δ_n^β from the value predicted by Cahn's rule, which is $(\xi_{n+1}^\alpha - \xi_n^\alpha)/\lambda_0$. In our simulations, this deviation never exceeded 1° . Due to the finite interface width of the phase-field model, it is very difficult to measure angles directly at the trijunction points, and such small deviations cannot be resolved. Therefore, the procedure outlined above that uses the whole trajectory of a trijunction point is the only way to obtain quantitative information about the violation of Cahn's rule directly from the simulations. It should be emphasized, however, that while the deviation itself is small, since the growth angle δ_n^β is itself small, the *ratio* of the two is not necessarily small. Indeed, it can be seen from Fig. 8 that the correction constitutes a sizable fraction of the growth angle. This explains why such a small deviation can induce quite large shifts in the stability spectrum.

The violation of Cahn's hypothesis explains the remaining discrepancies between our simulation results and the theory. To modify the theory by the inclusion of the corrective term in Eq. (30) seems possible, but is out of the scope of the present paper.

V. DYNAMICS OF COLONY FORMATION

To study the instabilities that lead to the formation of colonies, we constructed large arrays as described before, and perturbed the steady-state solution by a spatial displacement of the fields along the z direction. The amplitude of the displacement was a random variable of x with a white noise spectrum and an amplitude comparable to one lattice spacing. The goal was to study the initial instability of such random arrays as well as the nonlinear dynamics of well-developed colonies. The latter required long runs in big systems. The necessary computational power was attained by porting our simulation code on a parallel Cray T3E computer. We used a simple domain-decomposition scheme for parallelization, i.e., every processor calculated a part of the system. A load-balancing algorithm that adjusted the domain boundaries as a function of the computational load for each

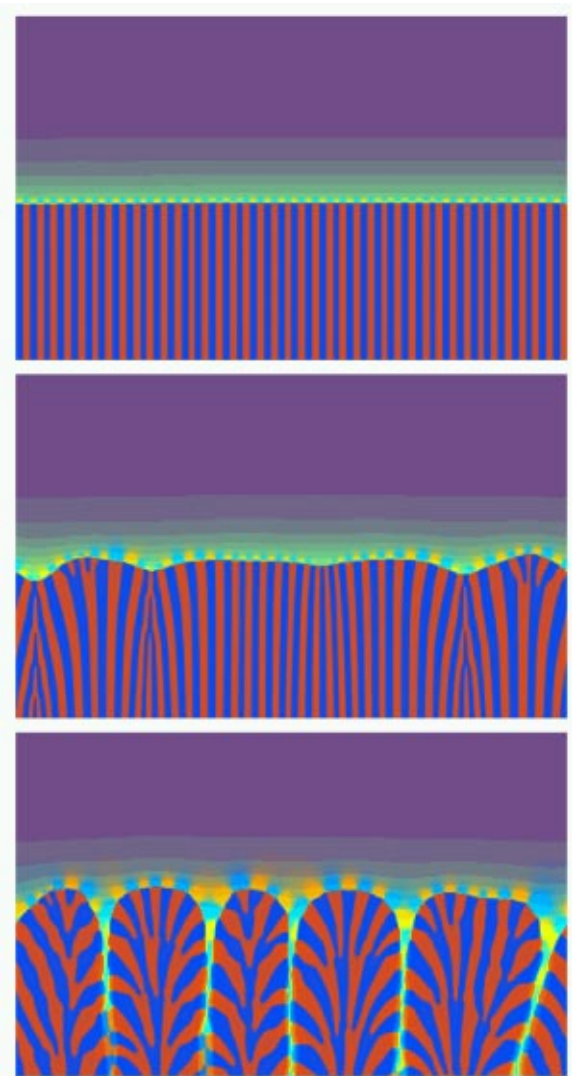


FIG. 12. (Color online) Snapshot pictures of a run with 40 lamella pairs at eutectic composition and $g=0.1$, $\Lambda=1.175$, and $w=0.2$. From top to bottom: $t/\tau=0$, 100 000, 375 000. In the liquid, the smooth contours ahead of the front represent isoconcentration lines of the ternary impurity; the small “halos” just in front of the growing lamellae are a visualization of the interlamellar (eutectic) diffusion field.

processor was used to optimize the yield.

For $u_\infty=0$ (eutectic composition), the initial evolution of the lamellar array is a linear superposition of the long-wavelength modes described in the preceding section. That is, if we decompose the set of trijunction displacements into Fourier modes, each mode grows with the (real or complex) growth rate that was determined in the single mode simulations of the preceding section. In Fig. 12, we show the resulting evolution for the same control parameters as in Fig. 6(a). The fastest growing mode is real with a wavelength of about $12\lambda_0$. Indeed, this mode dominates the interface shape in the second snapshot, where the first lamella termination events have occurred. At later times, the linear description becomes invalid. The further evolution is characterized by the growth of long protruding fingers, as can be seen in the

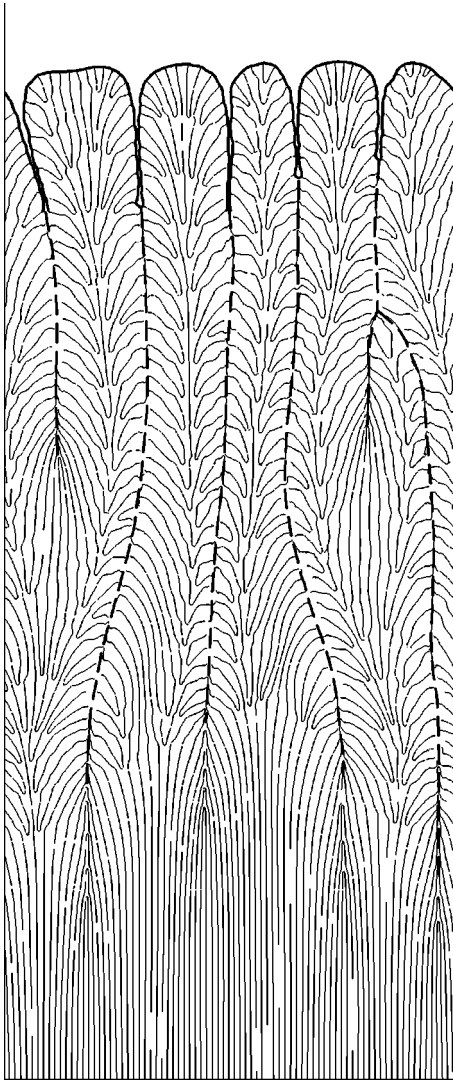


FIG. 13. Global view of the same run as in Fig. 12, without gray scale. Thin lines: solid-solid interfaces. Thick solid line: final solid-liquid interface. Thick dashed lines: trajectories of the grooves between fingers. There are two tip-splitting and one finger overgrowth events. Note the concave part of the final front in the center of the leftmost finger: a tip-splitting event will soon take place.

last snapshot picture. These fingers, however, do not reach a steady-state configuration up to the end of our simulation: their shape continuously changes, and there are some tip-splitting and overgrowth events. To highlight this feature, we show in Fig. 13 a complete plot of the whole solidified sample, where we have omitted the gray scale for clarity, and where we have marked the trajectories of the “deep grooves” between neighboring fingers. This run was performed on a lattice of size 1600×1200 and totals 15×10^6 iterations. On the Cray T3E, this run required about 3000 h single processor CPU time.

In Fig. 14, we show a run with again 40 lamella pairs, but now with both a larger temperature gradient and a larger initial spacing. Under these conditions, the instability develops more slowly, and the dispersion relation is entirely complex, such that we expect propagating or oscillatory modes.

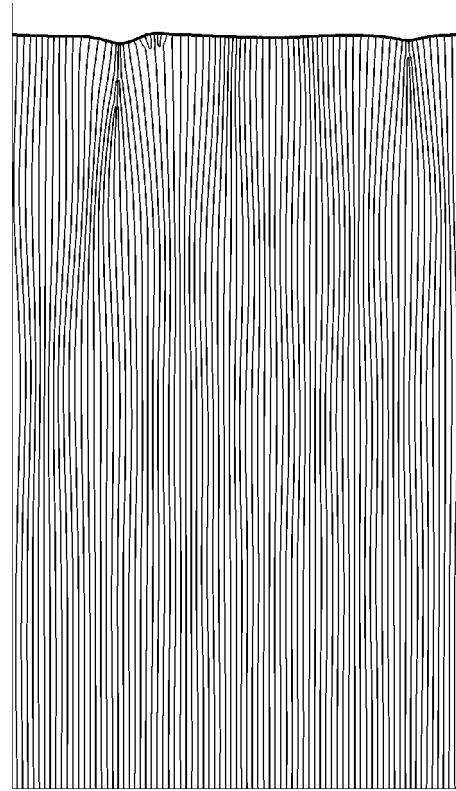


FIG. 14. Run with 40 lamella pairs at eutectic composition and $g=0.2$, $\Lambda=1.5$, and $w=0.2$. The dispersion relation is entirely complex, and oscillatory patterns appear. Thin lines: solid-solid interfaces. Thick solid line: final solid-liquid interface.

Indeed, on the right side of Fig. 14, there is an oscillatory “breathing mode” with wavelength about $10\lambda_0$, whereas on the left side, a traveling perturbation of the lamellar pattern can be seen. The run was not continued after the first lamella termination events, since the nonlinear regime is expected to lead to similar fingered patterns as in Fig. 12.

A quite different scenario occurs for off-eutectic compositions. An example is shown in Fig. 15. The linear regime is still in good agreement with the predictions of Ref. [23]. In particular, for sufficiently off-eutectic compositions, the impurity-induced long-wavelength instability competes with the 2λ -oscillatory (2λ -O) instability that is already present in binary eutectics. For the temperature gradient and impurity content chosen in our example, the long-wavelength instability is stationary and faster than the 2λ -O instability. Indeed, we find that the Fourier spectrum of the trijunction displacements is initially dominated by the smooth long-wavelength modes, while the 2λ -O instability develops much more slowly. However, as soon as the instability becomes “visible,” that is, the amplitude of the perturbation exceeds $\sim 0.1\Lambda_0$, localized fingerlike structures develop around a lamella of the minority phase and rapidly grow ahead of the front. The fine lamellae act almost as “guides” for the well-developed fingers during the subsequent evolution. In particular, note the long minority lamella that is like a “spine” for the rightmost finger in the third snapshot (we remind the reader that we use periodic boundary conditions in the lateral directions; hence, this is not a “wall effect”).

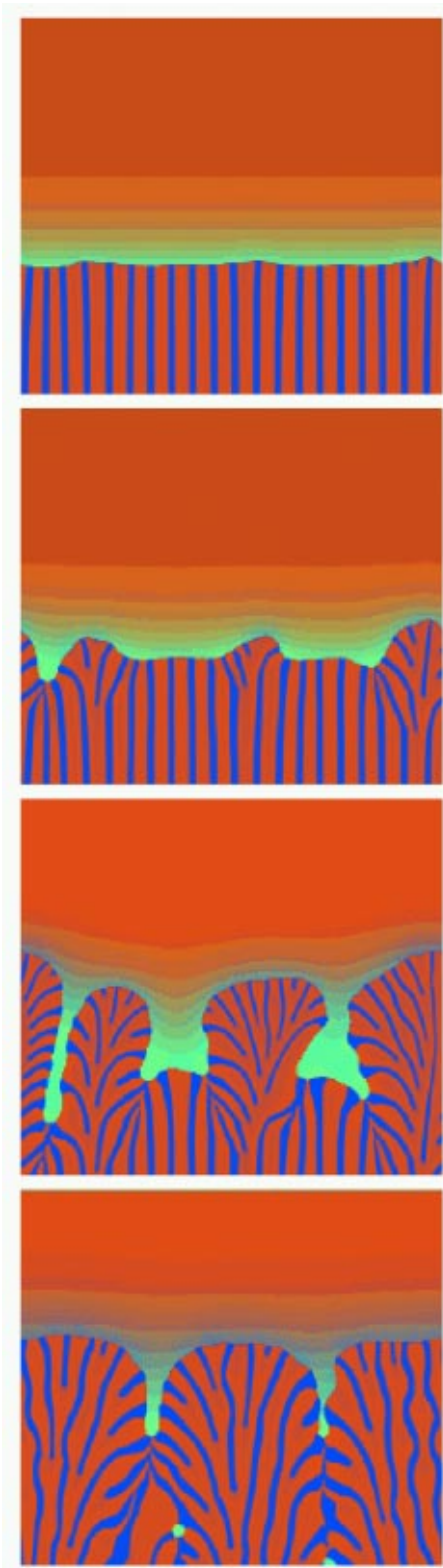


FIG. 15. (Color online) Snapshot pictures of a run with 20 lamella pairs at off-eutectic composition ($u_\infty=0.3$), $g=0.1$, $w=0.2$, and $\lambda_0/W=56$. From top to bottom: $t=85\,000$, $105\,000$, $125\,000$, $225\,000$ (in units of τ).

These structures, however, are only transient. In the final stage, when the colonies are well developed, they have rather flat tops and sharper “corners” than the fingers at eutectic composition. In the flat parts at the center of the colonies, sometimes a 2λ - O mode develops until it generates some new lamellae and dies out.

Structures such as the initial localized fingers are evidently nonlinear. It thus appears that the linear regime of the instability is much shorter for off-eutectic than for eutectic compositions. It is presently unclear what precisely triggers the formation of such fingers, and under which conditions they can form. In view of the necessary computer time, we did not carry out a detailed study to clarify these issues.

VI. CONCLUSIONS

We have presented a phase-field model for eutectic solidification in the presence of ternary impurities. This model has enabled us to carry out large-scale simulations of colony formation starting from arrays of up to 40 lamellae pairs.

In the linear regime, i.e., for small perturbations of the unstable steady-state growth front, these simulations have allowed us to critically test our previous linear stability analysis [23]. We find a good overall agreement with our theoretical predictions. Furthermore, a detailed treatment of the simulation data has allowed us to check the assumptions made in the linear stability analysis, and to precisely pinpoint the reasons for the differences between the theory and simulation results.

The most interesting conclusion is that the growth of the lamellae is not exactly normal to the large-scale envelope of the composite interface, a rule originally proposed by Cahn and used in the subsequent stability studies by Datye-Langer [6] and ourselves [23]. The motion of the trijunction points can be roughly understood as a superposition of normal motion as stipulated by Cahn’s rule and a slow “sliding” of the trijunctions along the front with a sideways velocity that is proportional to the gradient of the local lamellar spacing. Equivalently, this motion can be understood as a diffusion of the local lamellar spacing (phase diffusion); it hence tends to stabilize the front. In mathematical terms, it gives a new positive contribution to the phase-diffusion coefficient [44] that scales as $v_p \lambda_0^2 / \lambda_{\min}$, or equivalently, as $D \Delta \text{Pe}$. This effect seems to be qualitatively different from the corrections to the phase-diffusion coefficient reported previously in theoretical studies of binary eutectics submitted to a strong temperature gradient [45,46]. The resulting deviations of the growth angles from 90° are very small (below 1°). Hence, a direct measurement of this effect in experiments is impossible, since a precise measurement of the growth angles is complicated by crystallographic effects, in particular, the anisotropies of the surface tensions [18]. However, the growth rates of the long-wavelength modes are very sensitive to a small change in this angle. This is especially important for binary eutectics, where the impurity-driven morphological instability is absent. Indeed, it was recently found [36] that the new contribution to the phase-diffusion coefficient leads to a large and experimentally detectable effect on the critical wavelength for the onset of the long-wavelength

lamella elimination instability in binary eutectics.

Regarding the dynamics of fully developed colonies, we find that after the destabilization of the planar front, the array of two-phase cells undergoes a complicated and seemingly chaotic sequence of tip-splitting and cell elimination events. We were unable, in our simulations, to attain a steady-state configuration of the large-scale pattern, that is, the envelope of the front. This result is consistent with the fact that mono-phase cellular arrays in directional solidification of dilute alloys are unstable in the absence of crystalline anisotropy [38,37]. In fact, the lack of stability of the eutectic colonies in the absence of anisotropy suggests that the large-scale composite eutectic interface behaves qualitatively as a mono-phase front even beyond the linear regime. In this analogy, the addition of solid-liquid or solid-solid anisotropy could potentially produce an effective anisotropy of the composite interface that stabilizes its large-scale envelope. The quantitative exploration of this analogy, however, is far beyond the scope of the present work.

Regarding the comparison between our simulations and the experimental observations of Ref. [18], we find many similarities. In particular, we find in the simulations the oscillatory unstable modes predicted by our stability analysis. Such wavy structures are also observed in the experiments. We also find that well-developed two-phase cells do not seem to reach a steady state up to the largest times simulated. This is in agreement with the experiments, where no steady state has been reached even on length and time scales far superior to the range of our simulations (compare our Fig. 13 with Fig. 14 of Ref. [18]).

A number of experimental observations, however, remain to be understood. First, unstable modes in the experiments are sometimes manifested as waves that are emitted by localized perturbations, such as grain boundaries. These waves can propagate along the front, which remains planar, rather than be a transient that precedes colony formation. Some of these propagating waves seem to have characteristics of solitary waves. No such structures have been observed in our simulations. Furthermore, we observe some localized two-phase fingers that play a role during the instability of planar fronts at off-eutectic compositions, and that are similar to structures seen in the experiments (compare, in particular, our Fig. 15 with Fig. 6 of Ref. [18]). However, other experimentally observed patterns, such as “multiplet fingers” and two-phase dendrites are not reproduced by our simulations. It is possible that the existence of such patterns depends sensitively on the structure of the eutectic phase diagram, in particular, on the asymmetry of the two solid phases and their surface energies that have been shown to influence the stability of binary lamellar eutectics [7], and on crystalline anisotropy.

The present phase-field model could easily be modified to include some degree of asymmetry between phases as well as both solid-liquid and solid-solid anisotropy. In addition, the use of more general phase-field models with several order parameters [32–35], as well as the use of more efficient phase-field formulations [29] and numerical algorithms [47,48] that greatly enhance the accessible length and time scales, could help to elucidate these questions in the future.

The exploration of the enormously vast parameter space of growth conditions and material properties that govern the formation of complex two-phase microstructures remains, however, a formidable numerical task.

ACKNOWLEDGMENTS

This research was supported by U.S. DOE Grant No. DE-FG02-92ER45471 and benefited from computer time at the National Energy Research Scientific Computing Center (NERSC), Lawrence Berkeley National Laboratory, and at the Northeastern University Advanced Scientific Computation Center (NU-ASCC). We thank Silvère Akamatsu and Gabriel Faivre for many stimulating discussions.

APPENDIX: PHASE DIAGRAM AND SHARP-INTERFACE LIMIT OF THE PHASE-FIELD MODEL

Here, we show how to choose the parameters of the phase-field model in order to obtain a suitable phase diagram, and we relate the phase-field model to the classic free-boundary formulation of solidification. Our starting point is Eq. (3). For the free energies of the solid and liquid phases, f_{sol} and f_{liq} , we take

$$f_{\text{liq}}(u, \bar{c}, T) = u^2/2 + b(\bar{c} \ln \bar{c} - \bar{c}) - \epsilon_l \bar{c}, \quad (\text{A1})$$

$$f_{\text{sol}}(u, \bar{c}, T) = a(u^2 - 1)^2 + b(\bar{c} \ln \bar{c} - \bar{c}) - \epsilon_s \bar{c} - \alpha \Delta T / T_E, \quad (\text{A2})$$

where $\Delta T = T_E - T$ is the undercooling with respect to the binary eutectic point, and a , b , ϵ_s , ϵ_l , and α are constants. This choice is motivated by the following considerations. Since there are two solid phases, f_{sol} must have a double-well structure in u ; in contrast, f_{liq} has a single well. Without impurities ($\bar{c}=0$), at the eutectic temperature all three phases must have the same free energy; for $T > T_E$ ($T < T_E$), the liquid minimum must be below (above) the solid minima. This is conveniently achieved by the last term on the right-hand side of Eq. (A2) that simply shifts f_{sol} with respect to f_{liq} ; formally, α is equivalent to the latent heat.

The impurity terms have a form that is equivalent to the dilute limit of a regular solution model. Indeed, the terms containing \bar{c} correspond to the dilute approximations for the entropy of mixing and the energy cost of the impurities, respectively, with ϵ_v representing the difference in bond energies upon replacing a solvent atom by an impurity in phase v . The constant b , which sets the energy scale, should formally be proportional to the temperature. Since we are, however, only interested in a narrow temperature range around T_E , we simply use a constant.

The various coefficients can be related to physical quantities through the construction of a phase diagram. The conditions for thermodynamic equilibrium between two distinct phases are (i) equal chemical potentials for the eutectic components, (ii) equal chemical potentials for the ternary impurity, and (iii) equal grand potential, i.e.,

$$\mu_s \equiv \partial f_{\text{sol}} / \partial u|_{u_s} = \mu_l \equiv \partial f_{\text{liq}} / \partial u|_{u_l}, \quad (\text{A3})$$

$$\tilde{\mu}_s \equiv \partial f_{\text{sol}} / \partial \tilde{c}_s = \tilde{\mu}_l \equiv \partial f_{\text{liq}} / \partial \tilde{c}_l, \quad (\text{A4})$$

$$\Omega_s \equiv f_{\text{sol}} - \mu_s u_s - \tilde{\mu}_s \tilde{c}_s = \Omega_l \equiv f_{\text{liq}} - \mu_l u_l - \tilde{\mu}_l \tilde{c}_l, \quad (\text{A5})$$

where u_ν and \tilde{c}_ν , $\nu = s, l$, denote the equilibrium concentrations in solid and liquid. These conditions can be geometrically described as a ‘‘common tangent plane’’ to the free energy surface, analogous to the well-known double-tangent construction for binary alloys. From Eq. (A4), we get at once the standard partition relation for a dilute alloy,

$$\tilde{c}_s = K \tilde{c}_l, \quad (\text{A6})$$

with a partition coefficient given by

$$K = \exp[-(\epsilon_s - \epsilon_l)/b]. \quad (\text{A7})$$

Next, from Eq. (A3), under the assumption $\Delta T/T_E \ll 1$ (i.e., for temperatures close to the eutectic temperature), we have $u_l \ll 1$ and $u_s \approx \pm 1$, and we get

$$u_s = \frac{u_l}{8a} \pm 1, \quad (\text{A8})$$

where the two signs correspond to the two distinct solid-liquid equilibria. Finally, using Eqs. (A5), (A6), and (A8), we obtain

$$\alpha \Delta T/T_E = b(1-K)\tilde{c}_l \pm u_l. \quad (\text{A9})$$

Using the definition of ΔT , this can be rewritten as

$$T = T_E \pm m_u u_l - \tilde{m} \tilde{c}_l, \quad (\text{A10})$$

where m_u and \tilde{m} are the magnitudes of the liquidus slopes for the eutectic components and the impurity, respectively,

$$m_u = \left| \frac{dT}{du_l} \right| = \frac{T_E}{\alpha}, \quad (\text{A11})$$

$$\tilde{m} = \left| \frac{dT}{d\tilde{c}_l} \right| = \frac{b(1-K)T_E}{\alpha}. \quad (\text{A12})$$

Note that the scaled liquidus slope m_u can be related to the ‘‘true’’ liquidus slope m in the phase diagram with the help of Eq. (1),

$$m_u = m(c_\beta - c_\alpha)/2. \quad (\text{A13})$$

The parameter a controls the ratio of the liquidus and solidus slopes in the eutectic phase diagram; for simplicity, we will fix in the following $a = 1/8$, which gives a concentration jump across the interface that is independent of temperature (parallel liquidus and solidus lines). The parameter b , together with the partition coefficient K , fixes the ratio of eutectic and impurity liquidus slopes, $\tilde{m}/m_u = b(1-K)$.

When the thickness of the diffuse interfaces is much smaller than all other physical length scales, and in particular the lamellar spacing λ , the above phase-field equations can be related to the more conventional sharp-interface equations

of the macroscopic models of solidification by the technique of matched asymptotic expansions. This procedure has been detailed in several publications for models that are similar to ours, and hence we will only outline the results. Each solid has to reject its minority component and the ternary impurity into the liquid in order to grow. Since the concentrations are locally conserved quantities, mass balance at the interface implies that they obey boundary conditions of Stefan type at the moving boundary, i.e.,

$$-D \partial_n u = v_n (u_l - u_s), \quad (\text{A14})$$

$$-\tilde{D} \partial_n \tilde{c} = v_n (1-K)\tilde{c}_l. \quad (\text{A15})$$

Here, v_n and ∂_n are the normal velocity of the interface and the derivative normal to the interface, and u_l , u_s , and \tilde{c}_l are the values of the concentrations at the liquid and solid sides of the interface, respectively. These equations are valid for both solid-liquid interfaces; note that on the α -liquid interface, $u_l - u_s > 0$, whereas on the β -liquid interface, $u_l - u_s < 0$. The concentrations at the interface are related to temperature, shape, and speed of the interface by a generalized Gibbs-Thomson condition,

$$T = T_E \mp m_u u_l - \tilde{m} \tilde{c}_l - \Gamma \mathcal{K} - v_n / \mu_k, \quad (\text{A16})$$

where the upper (lower) sign is for the α (β) phase, the liquidus slopes m_u and \tilde{m} are given by Eqs. (A11) and (A12), Γ is the Gibbs-Thomson coefficient, \mathcal{K} is the local curvature of the interface, μ_k is the linear kinetic coefficient, and the concentrations on the solid side are linked to those on the liquid side via Eqs. (A6) and (A8). Without the last (kinetic) term, Eq. (A16) is a statement of local equilibrium at the interface, including capillary effects. The Gibbs-Thomson coefficient Γ is given in physical units by $\Gamma = \gamma_{sl} T_E / L$, where γ_{sl} is the surface tension of the solid-liquid interface, and L is the latent heat of melting. In the units of our model, this becomes

$$\Gamma = \gamma_{sl} T_E / \alpha. \quad (\text{A17})$$

The surface tension γ_{sl} is obtained as in Ref. [30] by first solving numerically the one-dimensional stationary versions of the equations of motion to obtain the interface profiles, and then computing the excess free energy per unit surface by inserting the profiles into the free energy functional. Note that, since the free energy density is taken dimensionless here, surface tensions have units of length. The solid-solid surface tension can be calculated analytically since along the $\alpha\beta$ interface $\phi \equiv 1$, and we obtain $\gamma_{ss} = (2/3)W_u$.

From the surface tensions, we can determine the contact angle θ , that is, the angle between the horizontal and the solid-liquid interfaces at a trijunction point where the solid-solid interface is vertical. Using Young’s condition of mechanical equilibrium, we get

$$\sin \theta = \frac{\gamma_{ss}}{2\gamma_{sl}}. \quad (\text{A18})$$

We have not explicitly calculated the value of the kinetic coefficient μ_k that appears in the last term of Eq. (A16). This would require to compute several integrals in the coupled variables u and ϕ through the solid-liquid interface (see Ref. [28] for more details in a simpler case), which can only be done numerically. Furthermore, we have neglected in the above analysis other nonequilibrium effects, and, in particular, solute trapping [49] that is generally present in phase-field models for alloy solidification [29,50]. It is known that solute trapping modifies the compositions on both the liquid

and the solid sides of a moving interface. This generates correction terms both in the Gibbs-Thomson condition and the mass balance relations, Eqs. (A15) and (A16). However, these corrections are proportional to the interface velocity, and are expected to be small for the range of solidification speeds used in our present simulations. Indeed, our simulation results indicate that the nonequilibrium effects are not entirely negligible; however, they are not important enough to justify a detailed analysis that would be quite involved [29].

-
- [1] W. Kurz and D.J. Fisher, *Fundamentals of Solidification* (Trans Tech, Aedermannsdorf, Switzerland, 1992).
- [2] M. Hillert, *Jernkontorets Ann.* **141**, 773 (1957).
- [3] K.A. Jackson and J.D. Hunt, *Trans. Metall. Soc. AIME* **236**, 1129 (1966).
- [4] W.H. Brandt, *J. Appl. Phys.* **16**, 139 (1945).
- [5] C. Zener, *Trans. Metall. Soc. AIME* **167**, 550 (1946).
- [6] V. Datye and J.S. Langer, *Phys. Rev. B* **24**, 4155 (1981).
- [7] A. Karma and A. Sarkissian, *Metall. Trans. A* **27**, 635 (1996); A. Sarkissian, Ph. D. thesis, Northeastern University, Boston, 1996.
- [8] M. Ginibre, S. Akamatsu, and G. Faivre, *Phys. Rev. E* **56**, 780 (1997).
- [9] H.W. Weart and D.J. Mack, *Trans. Metall. Soc. AIME* **212**, 664 (1958).
- [10] J.P. Chilton and W.C. Winegard, *J. Inst. Met.* **89**, 162 (1961).
- [11] R.W. Kraft and D.L. Albright, *Trans. Metall. Soc. AIME* **221**, 95 (1961).
- [12] J.D. Hunt and K.A. Jackson, *Trans. Metall. Soc. AIME* **236**, 843 (1966).
- [13] J.E. Gruzleski and W.C. Winegard, *J. Inst. Met.* **96**, 304 (1968); *Trans. Metall. Soc. AIME* **242**, 1785 (1968).
- [14] W.M. Rumball, *Metallurgia* **78**, 141 (1968).
- [15] P.K. Rohatgi and C.M. Adams, *Trans. Metall. Soc. AIME* **245**, 1609 (1969).
- [16] J.B. Bullock, C.J. Simpson, J.A. Eady, and W.C. Winegard, *J. Inst. Met.* **99**, 212 (1971).
- [17] M.D. Rinaldi, R.M. Sharp, and M.C. Flemings, *Metall. Trans.* **3**, 3133 (1972).
- [18] S. Akamatsu and G. Faivre, *Phys. Rev. E* **61**, 3757 (2000).
- [19] S.H. Han and R. Trivedi (unpublished).
- [20] W.A. Tiller, in *Liquid Metals and Solidification* (American Society of Metals, Cleveland, 1958).
- [21] D.G. McCartney, J.D. Hunt, and R.M. Jordan, *Metall. Trans. A* **11**, 1243 (1980).
- [22] W.W. Mullins and R.F. Sekerka, *J. Appl. Phys.* **3**, 444 (1964).
- [23] M. Plapp and A. Karma, *Phys. Rev. E* **60**, 6865 (1999).
- [24] J.S. Langer, in *Directions in Condensed Matter*, edited by G. Grinstein and G. Mazenko (World Scientific, Singapore, 1986), p. 164.
- [25] G.J. Fix, in *Free Boundary Problems: Theory and Applications*, edited by A. Fasano and M. Primicerio (Pitman, Boston, 1983), Vol. II, p. 580.
- [26] J.B. Collins and H. Levine, *Phys. Rev. B* **31**, 6119 (1985).
- [27] A.A. Wheeler, W.J. Boettinger, and G.B. McFadden, *Phys. Rev. A* **45**, 7424 (1992).
- [28] A. Karma and W.-J. Rappel, *Phys. Rev. E* **57**, 4323 (1998).
- [29] A. Karma, *Phys. Rev. Lett.* **87**, 115701 (2001).
- [30] A. Karma, *Phys. Rev. E* **49**, 2245 (1994).
- [31] K.R. Elder, F. Drolet, J.M. Kosterlitz, and M. Grant, *Phys. Rev. Lett.* **72**, 677 (1994).
- [32] A.A. Wheeler, G.B. McFadden, and W.J. Boettinger, *Proc. R. Soc. London, Ser. A* **452**, 495 (1996).
- [33] J. Tiaden, B. Nestler, H.-J. Diepers, and I. Steinbach, *Physica D* **115**, 73 (1998).
- [34] B. Nestler and A.A. Wheeler, *Physica D* **138**, 114 (2000).
- [35] T.S. Lo, A. Karma, and M. Plapp, *Phys. Rev. E* **63**, 031504 (2001).
- [36] S. Akamatsu, M. Plapp, G. Faivre, and A. Karma, *Phys. Rev. E* **66**, 030501 (2002).
- [37] S. Akamatsu, G. Faivre, and T. Ihle, *Phys. Rev. E* **51**, 4751 (1995).
- [38] P. Koczyński, W.-J. Rappel, and A. Karma, *Phys. Rev. Lett.* **77**, 3387 (1996).
- [39] Note that this definition of u differs by the factor of 1/2 in the denominator from the definition of the scaled concentration widely used in the literature.
- [40] By this we understand the Helmholtz free energy, normalized by a typical value of the free energy density times the total volume of the system.
- [41] J.A. Warren and J.S. Langer, *Phys. Rev. E* **47**, 2702 (1993).
- [42] J.W. Cahn and J.E. Hilliard, *J. Chem. Phys.* **28**, 258 (1958).
- [43] R.F. Almgren, *SIAM (Soc. Ind. Appl. Math.) J. Appl. Math.* **59**, 2086 (1999).
- [44] J.S. Langer, *Phys. Rev. Lett.* **44**, 1023 (1980).
- [45] K. Brattkus, B. Caroli, C. Caroli, and B. Roulet, *J. Phys. (France)* **51**, 1847 (1990); B. Caroli, C. Caroli, and B. Roulet, *ibid.* **51**, 1865 (1990).
- [46] Y.-J. Chen and S.H. Davis, *Acta Mater.* **49**, 1363 (2001).
- [47] N. Provatas, N. Goldenfeld, and J. Dantzig, *Phys. Rev. Lett.* **80**, 3308 (1998); *J. Comput. Phys.* **148**, 265 (1999).
- [48] M. Plapp and A. Karma, *Phys. Rev. Lett.* **84**, 1740 (2000); *J. Comput. Phys.* **165**, 592 (2000).
- [49] M.J. Aziz, *J. Appl. Phys.* **53**, 1158 (1982).
- [50] A.A. Wheeler, W.J. Boettinger, and G.B. McFadden, *Phys. Rev. E* **47**, 1893 (1993).